

Coexisting electronic smectic liquid crystal and superconductivity in a Si square-net semimetal

Christopher J. Butler,^{1,*} Toshiya Ikenobe,² Ming-Chun Jiang,^{1,3} Daigorou Hirai,⁴ Takahiro Yamada,⁵ Guang-Yu Guo,^{3,6} Ryotaro Arita,^{1,7} Tetsuo Hanaguri,^{1,†} and Zenji Hiroi²

¹RIKEN Center for Emergent Matter Science, 2-1 Hirosawa, Wako, Saitama 351-0198, Japan

²Institute for Solid State Physics, The University of Tokyo, Kashiwa, Chiba 277-8581, Japan

³Department of Physics and Center for Theoretical Physics,

National Taiwan University, Taipei 10617, Taiwan

⁴Department of Applied Physics, Nagoya University, Nagoya, Aichi 464-8603, Japan

⁵Institute of Multidisciplinary Research for Advanced Materials,

Tohoku University, Sendai, Miyagi 980-8577, Japan

⁶Physics Division, National Center for Theoretical Sciences, Taipei 10617, Taiwan

⁷Department of Physics, The University of Tokyo,

7-3-1 Hongo Bunkyo-ku, Tokyo 113-0033, Japan

Electronic nematic and smectic liquid crystals are spontaneous symmetry-breaking phases that are seen to precede or coexist with enigmatic unconventional superconducting states in multiple classes of materials. In this Letter we describe scanning tunneling microscopy observations of a short ranged charge stripe (smectic) order in NaAlSi, whose superconductivity is speculated to have an unconventional origin. As well as this we resolve a clear spatial modulation of the superconducting gap amplitude, which arises due to the intertwined superconducting and smectic orders. Numerical calculations help to understand the possible driving mechanism as a suppression of kinetic energy on the Fermi surface formed in part by two large, flat-topped hole pockets of *p*-orbital character.

Fluids of correlated electrons can spontaneously adopt liquid crystal-like distributions that break symmetries of the host crystal lattice. By analogy to ordinary liquid crystals, those that break the lattice's rotational symmetry are said to be nematic, while those that break both its rotational and translational symmetries are said to be smectic. A nematic electronic fluid was first proposed as a precursor to the superconducting state of a doped Mott insulator [1], and electronic liquid crystals more generally are thought to have a strong relationship, either competing or cooperative, with superconductivity (SC). They are observed to form within the *d* bands of several classes of cuprate and Fe-based high- T_c superconductors [2–5]. In the cuprates, scanning tunneling microscopy (STM) imaging famously shows that liquid crystal-like phases take on distinctive ‘checkerboard’ or short-ranged ladder-like configurations [6, 7]. In other *d*-orbital systems they are seen to adopt more-or-less uniaxial density-of-states modulations or charge stripe configurations [8–14].

Similar liquid crystal behavior in *s*- or *p*-orbital systems, which do not typically exhibit strong correlations, is not generally anticipated. Nevertheless, recent investigations of Sb-based square-net semimetals have shown anomalous charge ordered phases, other than charge density waves (CDWs), that can closely resemble the ladder-like ordered patterns seen in the cuprates despite their purer *p*-orbital character [15, 16]. The reason for apparently similar ordered phases in disparate *p*- and *d*-orbital systems and, for the *p* case in general, any potential re-

lationship between such ordered phases and SC, remain to be understood.

Here we use STM to examine NaAlSi, a nodal-line semimetal [17–20] and superconductor with bulk $T_c \approx 7.2$ K [21–24]. The relatively high T_c , especially given the small density-of-states around E_F , has led to speculation that its SC may have an unconventional origin [23]. However, this has been contested in other reports and there is a need for more detailed investigation [17, 21].

The structure of NaAlSi, depicted in Fig. 1(a), belongs to the space group *P4/nmm*, and cleavage results in flat Na-terminated surfaces with C_{4v} symmetry as shown in Fig. 1(b). Crystals of NaAlSi were synthesized and measured using STM as described in Appendix A. Tunneling conductance spectroscopy measured at the surface over a wide energy range, shown in Fig. 1(c), yields a curve broadly consistent with a semimetal. Figure 1(d) shows spectroscopy in a narrow range around E_F and at effective electron temperature $T_{\text{eff}} \approx 350$ mK. This shows fully gapped SC with $\Delta \approx 1$ meV.

Figure 1(e) shows a typical STM topograph of the Na-terminated surface. Although the atomic lattice cannot readily be observed, the lattice orientation can be established from faint Bragg peaks in the fast Fourier transform (FFT) of a conductance image (see below). To image the local density-of-states (LDOS) we first acquire tunneling conductance $\frac{dI}{dV}(\mathbf{r}, V)$ and, to mitigate artifacts of STM tip height variations, compute the normalized conductance $L(\mathbf{r}, V) = [\frac{dI}{dV}(\mathbf{r}, V)]/[I(\mathbf{r}, V)/V]$ [7, 25]. Figure 1(f) shows the image $L(\mathbf{r}, V = 5$ mV) in which we see charge stripe order with strong spatial fluctuations both in amplitude and in phase. The charge order seems to be weakly pinned: The stripe configuration can undergo abrupt local reconfigurations over time, un-

* christopher.butler@riken.jp

† hanaguri@riken.jp

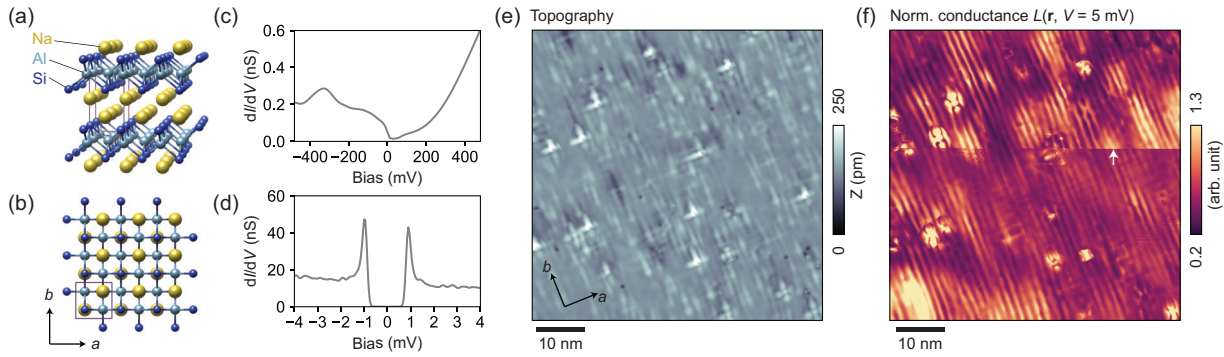


FIG. 1. Overview of the NaAlSi surface as seen using STM. (a) Depiction of the layered crystal structure and (b) top-down view of its Na-terminated cleaved surface, which has C_{4v} symmetry. Structures are depicted using VESTA [26]. (c) $\frac{dI}{dV}(V)$ conductance curve showing overall semimetallic behavior with a ‘v’-shaped minimum slightly above E_F ($V_{\text{set}} = 480$ mV, $I_{\text{set}} = 100$ pA, $V_{\text{mod}} = 10$ mV). (d) Conductance curve acquired around E_F , with effective temperature $T_{\text{eff}} \approx 350$ mK, showing the superconducting gap ($V_{\text{set}} = 50$ mV, $I_{\text{set}} = 250$ pA, $V_{\text{mod}} = 50$ μ V). (e) Typical STM topograph of the Na-terminated surface ($V_{\text{set}} = 30$ mV, $I_{\text{set}} = 100$ pA). The lattice vector orientations are marked with black arrows. (f) Image extracted at $V = 5$ mV from simultaneously acquired, normalized conductance ($V_{\text{mod}} = 0.5$ mV).

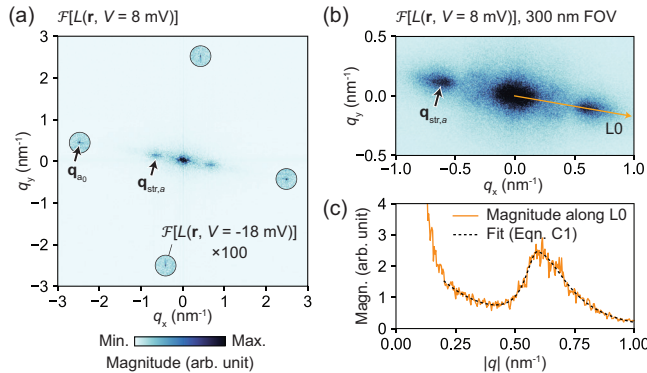


FIG. 2. Characterization of charge stripe order in q . (a) Fast Fourier transform (FFT) of $L(\mathbf{r}, V)$, written as $\mathcal{F}[L(\mathbf{r}, V)]$ ($V_{\text{set}} = 30$ mV, $I_{\text{set}} = 100$ pA, $V_{\text{mod}} = 0.5$ mV). The Bragg peaks, at \mathbf{q}_{a_0} , are not visible simultaneously with the stripes. They become visible only at particular energies and after enhancement of their intensity [100-fold in panel (a)]. The pair of lobes, one of which is marked as $\mathbf{q}_{\text{str},a}$, describe the charge stripes. (The subscript a denotes a direction parallel with the Bragg vector \mathbf{q}_{a_0} .) (b) A high-resolution view of the low- q region. [The source $L(\mathbf{r})$ images for both (a) and (b) are shown in Appendix B.] (c) The magnitude of $\mathcal{F}[L(\mathbf{r}, V = 8 \text{ mV})]$ sampled along linecut L0 in (b). The subsequent fitting procedure is described in Appendix C.

der ordinary scanning conditions. Such a reconfiguration is captured at the horizontal line marked with a white arrow. This fragility against external perturbations suggests that the order is likely to be purely electronic in origin.

We describe the charge stripe order more quantitatively by analyzing FFTs of $L(\mathbf{r}, V)$, denoted $\mathcal{F}[L(\mathbf{r}, V)]$. Figure 2(a) shows this for another cleaved surface. The Bragg vectors, and the wavevector that corresponds to the stripe order, are labeled as \mathbf{q}_{a_0} and $\mathbf{q}_{\text{str},a}$ respec-

tively. The lobes of intensity around $\mathbf{q}_{\text{str},a}$ have considerable width, and to better characterize them we obtain higher q resolution for another FFT by imaging $L(\mathbf{r}, V = 8 \text{ mV})$ over a $300 \times 300 \text{ nm}^2$ field-of-view. The resulting $\mathcal{F}[L(\mathbf{r}, V)]$ image is shown in Fig. 2(b). Using Lorentzian fitting (see Appendix C) to a linecut through $\mathcal{F}[L(\mathbf{r}, V)]$ parallel to \mathbf{q}_{a_0} , we estimate the central q vector of the aforementioned lobes, i.e. $\mathbf{q}_{\text{str},a}$. This gives $\mathbf{q}_{\text{str},a} \approx 0.235\mathbf{q}_{a_0}$, meaning that the period in the stripe-perpendicular direction is around $4.25a_0$ and the stripes are incommensurate with the lattice. (An observation of the detailed registry between charge stripe and atomic modulations is shown in Appendix D.) The same fitting procedure performed on similar data acquired on a second sample resulted in $\mathbf{q}_{\text{str},a} \approx 0.25\mathbf{q}_{a_0}$, so that the stripe periodicity was then around $4a_0$.

An interesting feature of the charge order is seen when we examine the energy dependence of the pattern in $\mathcal{F}[L(\mathbf{r}, V)]$, paying attention to the relative intensities near $\mathbf{q}_{\text{str},a}$ and its 90° -rotated partner, $\mathbf{q}_{\text{str},b}$. Figures 3(a) and 3(b) show $\mathcal{F}[L(\mathbf{r}, V)]$ images extracted above and below E_F . The image above E_F shows intensity at $\mathbf{q}_{\text{str},a}$ as described above. The image below E_F shows the coexistence of intensity around both $\mathbf{q}_{\text{str},a}$ and $\mathbf{q}_{\text{str},b}$. Figure 3(c) shows linecuts through $\mathcal{F}[L(\mathbf{r}, V)]$, taken parallel to $\mathbf{q}_{\text{str},a}$ and $\mathbf{q}_{\text{str},b}$. The energy-dependence curves for the total intensities around $\mathbf{q}_{\text{str},a}$ and $\mathbf{q}_{\text{str},b}$ are shown in Fig. 3(d). The stripe pattern of each orientation shows a distinct peak, one above and one below E_F , and with their intensity maxima separated by an energy of ~ 13 meV.

Figure 4(a) shows a large field-of-view L map featuring a domain wall (DW) between charge stripe domains that differ in orientation by 90° . The domains can be highlighted by obtaining Fourier amplitude maps extracted by filtering the FFT. This is done for the components around $\mathbf{q}_{\text{str},a}$ and $\mathbf{q}_{\text{str},b}$, and the resulting am-

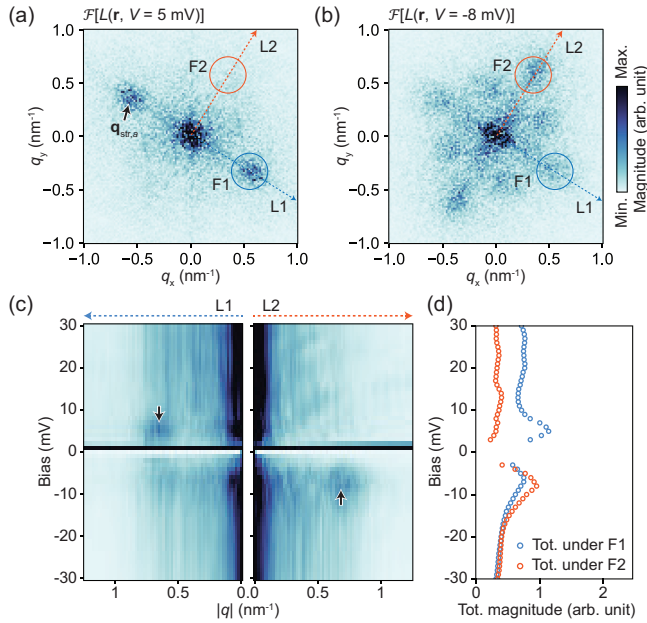


FIG. 3. Energy dependence of stripe intensity. (a) and (b) $\mathcal{F}[L(\mathbf{r})]$ images extracted above and below E_F , respectively ($V_{\text{set}} = 30$ mV, $I_{\text{set}} = 100$ pA, $V_{\text{mod}} = 0.5$ mV). (Source $L(\mathbf{r})$ images are shown in Appendix B.) (c) Linecuts through $\mathcal{F}[L(\mathbf{r}, V)]$ taken along the lines L1 and L2 marked in (a). Black arrows mark the features characterizing charge order. (d) The energy-dependence of total intensities under filters F1 and F2, located around the vector $\mathbf{q}_{\text{str},a}$ obtained by 2D Gaussian fitting to the image in (a), and around its 90° -rotated partner $\mathbf{q}_{\text{str},b}$, respectively. The values near E_F are removed due to severe noise resulting from the vanishing denominator in the normalization.

plitude maps are overlaid together in Fig. 4(b). A line-cut through these amplitude maps and $\frac{dI}{dV}(V)$ spectra acquired approximately along the same path are shown in Fig. 4(c) and (d). We see no obvious change in the SC gap size at the location of the DW, which by itself suggests neither a competitive nor cooperative relationship between charge stripe and SC orders. Most importantly, the existence of domains separated by a narrow DW suggests either spontaneous symmetry-breaking order if background strain is negligible or, at least, a high smectic susceptibility such that the stripe order shows a dramatic response to even a weakly varying strain field [27, 28].

We now examine the microscopic relationship between SC and charge stripe orders on the scale of the stripe period. Figures 5(a) and 5(b) show topographic and L images, respectively, in a small field-of-view. After measuring $\frac{dI}{dV}(\mathbf{r}, V)$ throughout this field-of-view, we extract linecuts perpendicular and parallel to the stripes [along the paths labeled in Fig. 5(a) as L4 and L5, respectively], and these are shown in Fig. 5(c) and 5(d). The SC coherence peaks show a subtle spatial modulation along the path perpendicular to the stripes, but are nearly uniform on the path along a single stripe. Figure 5(e) shows

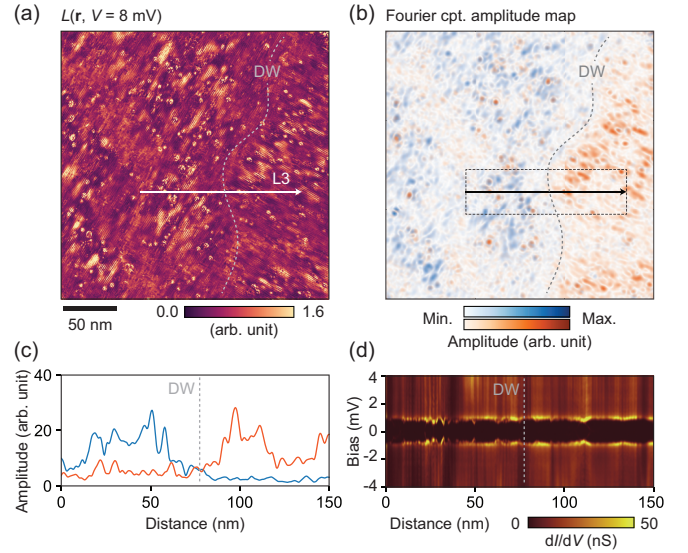


FIG. 4. Observation of domains of charge stripe order. (a) Large field-of-view L image exhibiting two domains of stripe order with differing orientations ($V_{\text{set}} = 30$ mV, $I_{\text{set}} = 100$ pA, $V_{\text{mod}} = 0.5$ mV). Fourier filtering is used to obtain amplitude maps for the Fourier components using filters similar to those in Fig. 3. The resulting maps are superimposed with separate color scales in (b). (c) Profiles through both amplitude maps [averaged over the short axis of the dashed rectangle in (b)], and (d) conductance measurement of the SC gap along the path L3 marked with a solid arrow ($V_{\text{set}} = 50$ mV, $I_{\text{set}} = 250$ pA, $V_{\text{mod}} = 50$ μ V, $T_{\text{eff}} \approx 350$ mK). The approximate DW location is marked with a gray dashed line.

selected $\frac{dI}{dV}(V)$ curves at the peaks and troughs of the modulation seen in Fig. 5(c), with locations indicated as blue and red dashed lines. The overall intensity of each $\frac{dI}{dV}(V)$ is location-dependent, and this dependence is affected by the varying STM tip height. Therefore, for ease of comparison the curves are each normalized according to the maximum conductance. (The segments of the curves at positive and negative bias are treated separately.) Figure 5(e) then shows a clear variation of the energy spacing between the upper and lower SC coherence peaks, namely 2Δ . In Fig. 5(f) we show the result of a phenomenological fit used to estimate and resolve the variation of $\Delta(\mathbf{r})$ (see Appendix E for details). The resulting variation of $\Delta(\mathbf{r})$ is shown in Fig. 5(f) alongside the value of $L(\mathbf{r}, V = 5$ mV) along the same path.

The modulation of the SC gap resembles some claimed observations of Cooper pair density wave phenomena [29, 30]. In systems where a prior CDW exists, the SC order parameter Δ is expected to have a spatially modulated component $\Delta(\mathbf{r})$ that follows the charge density modulation, having the same characteristic wavevector(s) [29, 31]. In that case the CDW can be said to be the primary order while the pair density wave is a subsidiary or secondary order. In the present case the primary order is not a CDW, but is instead liquid crystal-like, and so instead of a secondary pair density wave,

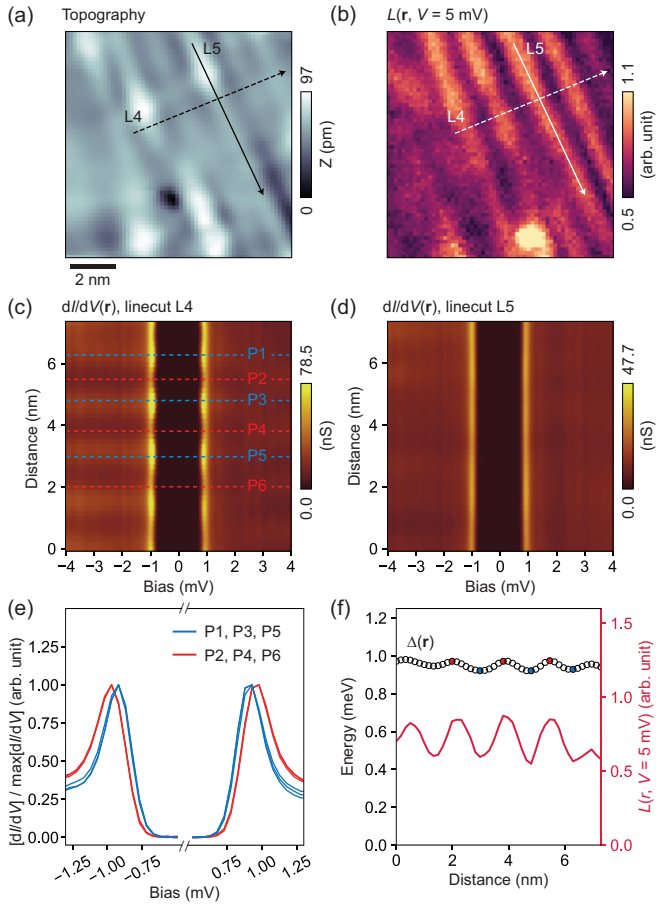


FIG. 5. Microscopic correspondence between charge stripe and SC orders. (a) A topograph ($V_{\text{set}} = 50$ mV, $I = 250$ pA) and (b) simultaneous L map in a small field of view. (c) and (d) Linecuts extracted from the simultaneous $\frac{dI}{dV}(V)$ conductance ($V_{\text{mod}} = 50$ μ V, $T_{\text{eff}} \approx 350$ mK), along paths L4 and L5 marked in both (a) and (b) with dashed and solid lines, respectively. (e) $\frac{dI}{dV}(V)$ curves sampled at the peaks and troughs of the modulation in (c). (f) The value of the local SC order parameter $\Delta(\mathbf{r}) = [|\Delta_{\text{UCP}}(\mathbf{r})| + |\Delta_{\text{LCP}}(\mathbf{r})|]/2$ (black circles) obtained using the fitting procedure described in Appendix E, and the corresponding variation of L along path L2. The modulations of $\Delta(\mathbf{r})$ and $L(\mathbf{r})$ are in phase.

the modulation of SC order here might be termed a secondary ‘pair liquid crystal’. In Fig. 5(f), L can be taken as a proxy for the local charge density, and it is then natural that the variation of $\Delta(\mathbf{r})$ follows that of $L(\mathbf{r})$.

To begin to understand the origin of the observed charge order, we calculate the surface electronic band structure using the density functional theory (DFT) framework as described in Appendix F. Figure 6(a) shows the calculated spectral function along high-symmetry lines of the surface Brillouin zone. The overall features of the surface bands are found not to differ substantially from those previously calculated for the bulk, because the bulk bands have fairly weak dispersion along the k_z axis [17, 22]. The salient features are a $\bar{\Gamma}$ -centered electron-like pocket of Al s -orbital origin and, also around

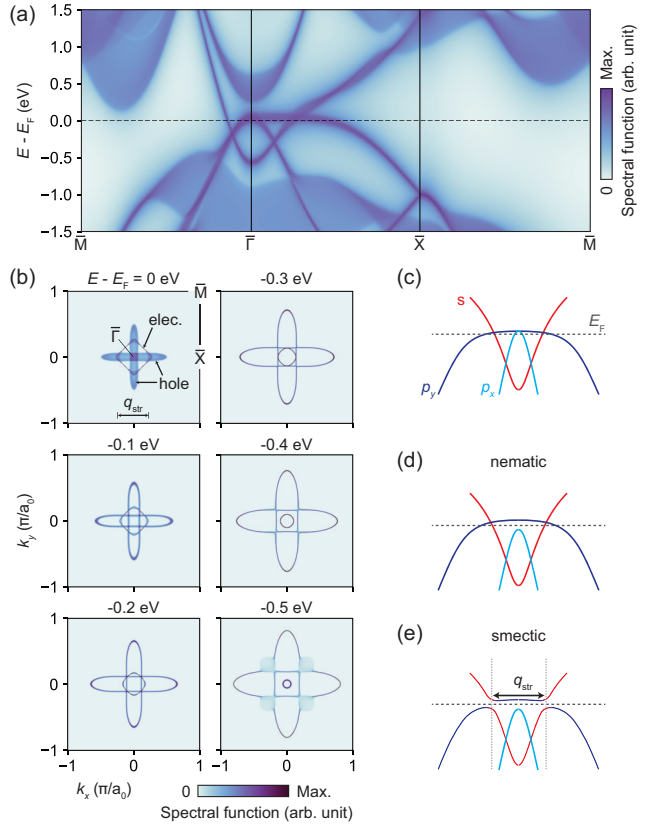


FIG. 6. Calculated surface spectral function for NaAlSi. (a) Spectral function plotted along the high-symmetry lines of the Brillouin zone. (b) Constant-energy cuts through the spectral function at selected, successively decreasing energies. The length of \mathbf{q}_{str} is indicated in the first panel. (c)–(e) Schematics of the band structure naïvely predicted using DFT, the band structure after lifting of the degeneracy between the p_x - and p_y -derived hole pockets, and after formation of stripe order.

$\bar{\Gamma}$, two large oblong hole pockets of Si p -orbital origin [17, 18, 22], which have orthogonal orientations and each extend along one of the $\bar{\Gamma}\text{X}$ axes. Notably, the hole pockets only slightly cross the Fermi level from below, and do so with a remarkably flat dispersion over a large range of k . Figure 6(b) shows selected constant-energy contours of the spectral function at E_F and at successively lower energies.

Lowering of rotational symmetry from C_{4v} to C_{2v} can be explained by a lifting of degeneracy between the p_x and p_y hole pockets, which are depicted schematically in Fig. 6(c), due to the band Jahn-Teller or an equivalent effect. This may be energetically favored due to the large energy saving available if the flat top of one hole pocket sinks below E_F . This would lead to a state that breaks the crystal’s rotational symmetry but retains its translational symmetry, as depicted in Fig. 6(d), namely a nematic state. Breaking of translational symmetry additionally requires that the band structure undergoes a reconstruction *via* a nesting-driven instability with the wavevector \mathbf{q}_{str} , and with this in mind we indicate its

length in the first panel of Fig. 6(b). This shows that \mathbf{q}_{str} closely matches the wavevector connecting regions along either $\overline{X\Gamma X}$ axis where the electron band crosses through the flat top of one of the hole bands. The appearance of a new periodicity with wavevector \mathbf{q}_{str} allows an effective shrinking of the Brillouin zone such that a gap can open at the new zone boundary. This then allows a gap to open where the electron and hole bands cross, as depicted in Fig. 6(e), leading to a further energy saving, and resulting in the observed smectic behavior. (This does not lead to an insulator because the bands cross E_F elsewhere in the Brillouin zone.) This scenario naturally explains why a clearer C_{2v} pattern is seen above E_F but a pattern with symmetry closer to C_{4v} is observed below [recall the pattern in Fig. 3(b), as compared to that in 3(a)]. Only one of the hole bands interacts with the electron band above E_F , resulting in stripes, while below E_F both hole bands do so.

In summary, we have described charge stripe order that breaks both rotational and translational symmetries of the host lattice. It is short-ranged, having a coherence length only a few times the modulation period (Appendix C), and its spatial fluctuations appear to be reconfigurable under mild electronic perturbation, as seen in Fig. 1(f). The observed phenomena are best described as a smectic liquid crystal-like behavior. Although the canonical phenomenologies for a smectic phase and a CDW partially overlap, the present observations would have to be interpreted as a very unusual CDW: It breaks rotational symmetry (unusual for CDWs unless accompanied by orthorhombicity [16]), it has exceptionally strong spatial fluctuations and, especially, its two orthogonal symmetry-breaking LDOS configurations reside at different energies. The smectic and SC orders are found to be intertwined such that the SC gap Δ is modulated in

phase with the striped LDOS, leading to an unusual secondary ‘Cooper pair liquid crystal’. Finally, we propose that the driving mechanism may involve a band Jahn-Teller-like lifting of degeneracy between p_x and p_y bands, incentivized by the large energy saving available due to the bands’ flat dispersion in proximity to E_F . This is followed by a nesting-driven instability where the remaining Fermi contour is crossed by the coexisting s band. This represents a rare case of electronic liquid crystal behavior in a p -orbital material, and extends investigations of the relationship between superconductivity and electronic liquid crystal behavior beyond the well-known d orbital examples.

ACKNOWLEDGEMENTS

We are grateful to T. Machida and M. Naritsuka for assistance, and to T. Nakamura, Y. Fujisawa, Y. Okada, S.-Y. Guan and T.-M. Chuang for helpful discussions. This work was supported by JSPS KAKENHI Grants No. JP20H02820, No. JP23H04860, No. JP25K21692, and No. JP25H01252, and also by a Grant-in-Aid for Scientific Research on Innovative Areas ‘Quantum Liquid Crystals’ (KAKENHI Grant No. JP19H05824 and No. JP19H05825). M.-C. J. acknowledges support from RIKEN’s IPA program.

DATA AVAILABILITY

The data that support the findings presented here are available from the corresponding authors upon reasonable request.

-
- [1] S. A. Kivelson, E. Fradkin, and V. J. Emery, *Electronic liquid-crystal phases of a doped Mott insulator*. *Nature* **393**, 550–553 (1998). <https://doi.org/10.1038/31177>
- [2] J. M. Tranquada, B. J. Sternlieb, J. D. Axe, Y. Nakamura, and S. Uchida, *Evidence for stripe correlations of spins and holes in copper oxide superconductors*. *Nature* **375**, 561–563 (1995). <https://doi.org/10.1038/375561a0>
- [3] M. J. Lawler, K. Fujita, J. Lee, A. R. Schmidt, Y. Kohsaka, C. K. Kim, H. Eisaki, S. Uchida, J. C. Davis, J. P. Sethna, and E.-A. Kim, *Intra-unit-cell electronic nematicity of the high- T_c copper-oxide pseudogap states*. *Nature* **466**, 347–351 (2010). <https://doi.org/10.1038/nature09169>
- [4] B. Keimer, S. A. Kivelson, M. R. Norman, S. Uchida, and J. Zaanen, *From quantum matter to high-temperature superconductivity in copper oxide*. *Nature* **518**, 179–186 (2015). <https://doi.org/10.1038/nature14165>
- [5] T. Shibauchi, T. Hanaguri, and Y. Matsuda, *Exotic Superconducting States in FeSe-based Materials*. *J. Phys. Soc. Jpn.* **89**, 102002 (2020). <https://doi.org/10.7566/JPSJ.89.102002>
- [6] T. Hanaguri, C. Lupien, Y. Kohsaka, D.-H. Lee, M. Azuma, M. Takano, H. Takagi, and J. C. Davis, *A ‘checkerboard’ electronic crystal state in lightly hole-doped $Ca_{2-x}Na_xCuO_2Cl_2$* . *Nature* **430**, 1001–1005 (2004). <https://doi.org/10.1038/nature02861>
- [7] Y. Kohsaka, C. Taylor, K. Fujita, A. Schmidt, C. Lupien, T. Hanaguri, M. Azuma, M. Takano, H. Eisaki, H. Takagi, S. Uchida, and J. C. Davis, *An intrinsic bond-centered electronic glass with unidirectional domains in underdoped cuprates*. *Science* **315**, 1380–1385 (2007). <https://doi.org/10.1126/science.1138584>
- [8] T.-M. Chuang, M. P. Allan, J. Lee, Y. Xie, N. Ni, S. L. Budko, G. S. Boebinger, P. C. Canfield, and J. C. Davis, *Nematic Electronic Structure in the ‘Parent’ State of the Iron-Based Superconductor $Ca(Fe_{1-x}Co_x)_2As_2$* . *Science* **327**, 181–184 (2010). <https://doi.org/10.1126/science.1181083>
- [9] C. M. Yim, C. Trainer, R. Aluru, S. Chi, W. N. Hardy, R. Liang, D. Bonn, and P. Wahl, *Discovery of a strain-stabilised smectic electronic order in LiFeAs*. *Nat.*

- Commun. **9**, 2602 (2018). <https://doi.org/10.1038/s41467-018-04909-y>
- [10] Y. Yuan, X. Fan, X. Wang, K. Han, Y. Zhang, Q.-K. Xue, and W. Li, *Incommensurate smectic phase in close proximity to the high- T_c superconductor $\text{FeSe}/\text{SrTiO}_3$* . Nat. Commun. **12**, 2196 (2021). <https://doi.org/10.1038/s41467-021-22516-2>
- [11] C. J. Butler, Y. Kohsaka, Y. Yamakawa, M. S. Bahramy, S. Onari, H. Kontani, T. Hanaguri, and S. Shamoto, *Correlation-driven electronic nematicity in the Dirac semimetal BaNiS_2* . Proc. Natl. Acad. Sci. **119** (49) e2212730119 (2022). <https://doi.org/10.1073/pnas.2212730119>
- [12] H. Li, S. Cheng, B. R. Ortiz, H. Tan, D. Werhahn, K. Zeng, D. Johrendt, B. Yan, Z. Wang, S. D. Wilson, and I. Zeljkovic, *Electronic nematicity without charge density waves in titanium-based kagome metal*. Nat. Phys. **19**, 1591–1598 (2023). <https://doi.org/10.1038/s41567-023-02176-3>
- [13] M. Naritsuka, I. Benedičić, L. C. Rhodes, C. A. Marques, C. Trainer, Z. Li, A. C. Komarek, and P. Wahl, *Compass-like manipulation of electronic nematicity in $\text{Sr}_3\text{Ru}_2\text{O}_7$* . Proc. Natl. Acad. Sci. **120** (36) e2308972120 (2023). <https://doi.org/10.1073/pnas.2308972120>
- [14] Y. Wang, H. Li, S. Cheng, H. Zhao, B. R. Ortiz, A. C. Salinas, S. D. Wilson, Z. Wang, and I. Zeljkovic, *Interplay of Nanoscale Strain and Smectic Susceptibility in Kagome Superconductors*. Phys. Rev. X **15**, 021074 <https://doi.org/10.1103/PhysRevX.15.021074>
- [15] B. Venkatesan, S.-Y. Guan, J.-T. Chang, S.-B. Chiu, P.-Y. Yang, C.-C. Su, T.-R. Chang, K. Raju, R. Sankar, S. Fongchaiya, M.-W. Chu, C.-S. Chang, G. Chang, H. Lin, A. del Maestro, Y.-J. Kao, and T.-M. Chuang, *Direct visualization of a disorder driven electronic smectic phase in nonsymmorphic square-net semimetal GdSbTe* . npj Quantum Mater. **10**, 56 (2025) <https://doi.org/10.1038/s41535-025-00779-y>
- [16] X. Que, Q. He, L. Zhou, S. Lei, L. Schoop, D. Huang, and H. Takagi, *Visualizing the internal structure of the charge-density-wave state in CeSbTe* . Nat. Commun. **16**, 3053 (2025). <https://doi.org/10.1038/s41467-025-58417-x>
- [17] L. Muechler, Z. Guguchia, J.-C. Orain, J. Nuss, L. M. Schoop, R. Thomale, and F. O. von Rohr, *Superconducting order parameter of the nodal-line semimetal NaAlSi* . APL Mater. **7**, 121103 (2019). <https://doi.org/10.1063/1.5124242>
- [18] X. Yi, W. Q. Li, Z. H. Li, P. Zhou, Z. S. Ma, and L. Z. Sun, *Topological dual double node-line semimetals $\text{NaAlSi}(\text{Ge})$ and their potential as cathode material for sodium ion batteries*. J. Mater. Chem. C **7**, 15375 (2019). <https://doi.org/10.1039/c9tc04096j>
- [19] C. Song, L. Jin, P. Song, H. Rong, W. Zhu, B. Lang, S. Cui, Z. Sun, L. Zhao, Y. Shi, X. Zhang, G. Liu, and X. J. Zhou, *Spectroscopic evidence for Dirac nodal surfaces and nodal rings in the superconductor NaAlSi* . Phys. Rev. B **105**, L161104 (2022). <https://doi.org/10.1103/PhysRevB.105.L161104>
- [20] S. Uji, T. Konoike, Y. Hattori, T. Terashima, T. Oguchi, T. Yamada, D. Hirai, T. Ikenobe, and Z. Hiroi, *Anomalous Diamagnetic Torque Signals in Topological Nodal-Line Semimetal NaAlSi* . J. Phys. Soc. Jpn. **92**, 074703 (2023). <https://doi.org/10.7566/JPSJ.92.074703>
- [21] S. Kuroiwa, H. Kawashima, H. Kinoshita, H. Okabe, and J. Akimitsu, *Superconductivity in ternary silicide NaAlSi with layered diamond-like structure*. Physica C **466**, 11–15 (2007) <https://doi.org/10.1016/j.physc.2007.04.232>
- [22] H. B. Rhee, S. Banerjee, E. R. Ylvisaker, and W. E. Pickett, *NaAlSi : Self-doped semimetallic superconductor with free electrons and covalent holes*. Phys. Rev. B **81**, 245114 (2020). <https://doi.org/10.1103/PhysRevB.81.245114>
- [23] T. Yamada, D. Hirai, H. Yamane, and Z. Hiroi, *Superconductivity in the Topological Nodal-line Semimetal NaAlSi* . J. Phys. Soc. Jpn. **90**, 034710 (2021). <https://doi.org/10.7566/JPSJ.90.034710>
- [24] R. Zhong, Z. Yang, Q. Wang, F. Zheng, W. Li, J. Wu, C. Wen, X. Chen, Y. Qi, and S. Yan, *Spatially Dependent in-Gap States Induced by Andreev Tunneling through a Single Electronic State*. Nano Lett. **24**, 8580–8586 (2024). <https://doi.org/10.1021/acs.nanolett.4c01581>
- [25] A. J. Macdonald, Y.-S. Tremblay-Johnston, S. Grothe, S. Chi, P. Dosanjh, S. Johnston, and S. A. Burke, *Dispersing artifacts in FT-STS: a comparison of set point effects across acquisition modes*. Nanotechnology **27**, 414004 (2016). [doi:10.1088/0957-4448/27/41/414004](https://doi.org/10.1088/0957-4448/27/41/414004)
- [26] K. Momma and F. Izumi, *VESTA 3 for three-dimensional visualization of crystal, volumetric and morphology data*. J. Appl. Crystallogr., **44**, 1272–1276 (2011). <https://doi.org/10.1107/S0021889811038970>
- [27] C. Guo, G. Wagner, C. Putzke, D. Chen, K. Wang, L. Zhang, M. Gutierrez-Amiga, I. Errea, M. G. Vergniory, C. Felser, M. H. Fischer, T. Neupert, and P. J. W. Moll, *Correlated order at the tipping point in the kagome metal CsV_3Sb_5* . Nat. Phys. **20**, 579 (2024). <https://doi.org/10.1038/s41567-023-02374-z>
- [28] C. J. Butler, M. Murase, S. Sawada, M.-C. Jiang, D. Hashizume, G.-Y. Guo, R. Arita, T. Hanaguri, and T. Sasagawa, *Valley Polarization of Landau Levels in the ZrSiS Surface Band Driven by Residual Strain*. Phys. Rev. X **15**, 011033 (2025). <https://doi.org/10.1103/PhysRevX.15.011033>
- [29] X. Liu, Y. X. Chong, R. Sharma, and J. C. S. Davis, *Discovery of a Cooper-pair density wave in a transition-metal dichalcogenide*. Science **372**, 1447–1452 (2021). <https://doi.org/10.1126/science.abd4607>
- [30] H. Chen, H. Yang, B. Hu, Z. Zhao, J. Yuan, Y. Xing, G. Qian, Z. Huang, G. Li, Y. Ye, S. Ma, S. Ni, H. Zhang, Q. Yin, C. Gong, Z. Tu, H. Lei, H. Tan, S. Zhou, C. Shen, X. Dong, B. Yan, Z. Wang, and H.-J. Gao, *Roton pair density wave in a strong-coupling kagome superconductor*. Nature **599**, 222–228 (2021) <https://doi.org/10.1038/s41586-021-03983-5>
- [31] K. Machida, T. Koyama, and T. Matsubara, *Theory of charge-density-wave superconductors*. Phys. Rev. B **23**, 99 (1981). <https://doi.org/10.1103/PhysRevB.23.99>
- [32] T. Hanaguri, *Development of high-field STM and its application to the study on magnetically tuned criticality in $\text{Sr}_3\text{Ru}_2\text{O}_7$* . J. Phys. Conf. Ser. **51**, 514 (2006). <https://doi.org/10.1088/1742-6596/51/1/117>
- [33] K. M. Thyng, C. A. Greene, R. D. Hetland, H. M. Zimberle, and S. F. DiMarco, *True Colors of Oceanography: Guidelines for Effective and Accurate Colormap Selection*. Oceanography **29**, 9–13 (2016). <https://doi.org/10.5670/oceanog.2016.66>

- [34] M. Naritsuka, T. Machida, S. Asano, Y. Yanase, and T. Hanaguri, *Superconductivity controlled by twist angle in monolayer NbSe₂ on graphene*. Nat. Phys. **21**, 746–753 (2025). <https://doi.org/10.1038/s41567-025-02828-6>
- [35] G. Kresse and J. Furthmüller, *Efficiency of ab-initio total energy calculations for metals and semiconductors using a plane-wave basis set*. Computational Materials Science **6**, 15–50, (1996). [https://doi.org/10.1016/0927-0256\(96\)00008-0](https://doi.org/10.1016/0927-0256(96)00008-0)
- [36] G. Kresse and J. Furthmüller, *Efficient iterative schemes for ab initio total-energy calculations using a plane-wave basis set*. Phys. Rev. B **54**, 11169 (1996). [10.1103/PhysRevB.54.11169](https://doi.org/10.1103/PhysRevB.54.11169)
- [37] P. E. Blöchl, *Projector augmented-wave method*. Phys. Rev. B **50**, 17953–17979 (1994). [10.1103/PhysRevB.50.17953](https://doi.org/10.1103/PhysRevB.50.17953)
- [38] G. Kresse and D. Joubert, *From ultrasoft pseudopotentials to the projector augmented-wave method*. Phys. Rev. B **59**, 1758 (1999). [10.1103/PhysRevB.59.1758](https://doi.org/10.1103/PhysRevB.59.1758)
- [39] J. P. Perdew, K. Burke, and M. Ernzerhof, *Generalized Gradient Approximation Made Simple*. Phys. Rev. Lett. **77**, 3865–3868 (1996). [10.1103/PhysRevLett.77.3865](https://doi.org/10.1103/PhysRevLett.77.3865)
- [40] G. Pizzi, V. Vitale, R. Arita, S. Blügel, F. Freimuth, G. Géranton, M. Gibertini, D. Gresch, C. Johnson, T. Koretsune, J. Ibañez-Azpiroz, H. Lee, J.-M. Lihm, D. Marchand, A. Marrazzo, Y. Mokrousov, J. I. Mustafa, Y. Nohara, Y. Nomura, L. Paulatto, S. Poncé, T. Ponweiser, J. Qiao, F. Thöle, S. S. Tsirkin, M. Wierzbowska, N. Marzari, D. Vanderbilt, I. Souza, A. A. Mostofi, and J. R. Yates, *Wannier90 as a community code: new features and applications*. Journal of Physics: Condensed Matter **32**, 165902 (2020). <https://doi.org/10.1088/1361-648X/ab51ff>
- [41] M. P. Lopez Sancho, J. M. Lopez Sancho, J. M. L. Sancho, and J. Rubio, *Highly convergent schemes for the calculation of bulk and surface Green functions*. Journal of Physics F: Metal Physics **15**, 851–858 (1985). <https://doi.org/10.1088/0305-4608/15/4/009>
- [42] Q. S. Wu, S.N. Zhang, H.-F. Song, M. Troyer, and A. A. Soluyanov, *WannierTools: An open-source software package for novel topological materials*. Comput. Phys. Commun. **224**, 405 (2018). <https://doi.org/10.1016/j.cpc.2017.09.033>

Appendix A: Crystal synthesis and STM measurements

Crystals were synthesized as described previously [23]. They were glued to sample plates, and prepared for later *in situ* cleavage, in a N₂ glovebox due to the rapid degradation upon exposure to air. They were then loaded into an ultra-high vacuum chamber ($P \sim 10^{-10}$ Torr) before cleaving at about 77 K, after which they were quickly inserted into a modified Unisoku USM1300 low-temperature STM system [32]. STM measurements were performed using electro-chemically etched tungsten tips that were characterized and conditioned using field ion microscopy followed by repeated mild indentation at a clean Cu(111) surface. Measurements were performed at $T = 1.5$ K unless otherwise stated in the relevant text.

Tunneling conductance was measured using the lock-in technique with bias modulation of frequency $f_{\text{mod}} = 617.3$ Hz and an amplitude V_{mod} specified in the caption describing each measurement. The effective electron temperature T_{eff} was estimated by fitting a Dynes curve to a $\frac{dI}{dV}(V)$ spectrum measured using a superconducting Al tip on Cu(111).

Topography maps, conductance maps and their Fourier transforms are plotted using perceptually uniform colormaps [33].

Appendix B: Source $L(\mathbf{r})$ images for $\mathcal{F}[L(\mathbf{r})]$ images displayed in Figs. 2 and 3

Figure 7. shows the $L(\mathbf{r})$ images used to obtain the Fourier transform results displayed in Figs. 2 and 3. Figures 7(a) and 7(b) show the small and large field-of-view data used to obtain the overview of q space in Fig. 2(a), and the high-resolution view of the low- q region in Fig. 2(b). Figures 7(c) and 7(d), acquired on a different sample, show the $L(\mathbf{r})$ images extracted for positive and negative energies in the same field-of-view, whose $\mathcal{F}[L(\mathbf{r})]$ images are shown in Fig. 3(a) and 3(b) above. As is indicated above for the $\mathcal{F}[L(\mathbf{r})]$ image, it is also clear from the $L(\mathbf{r})$ images that the LDOS adopts a

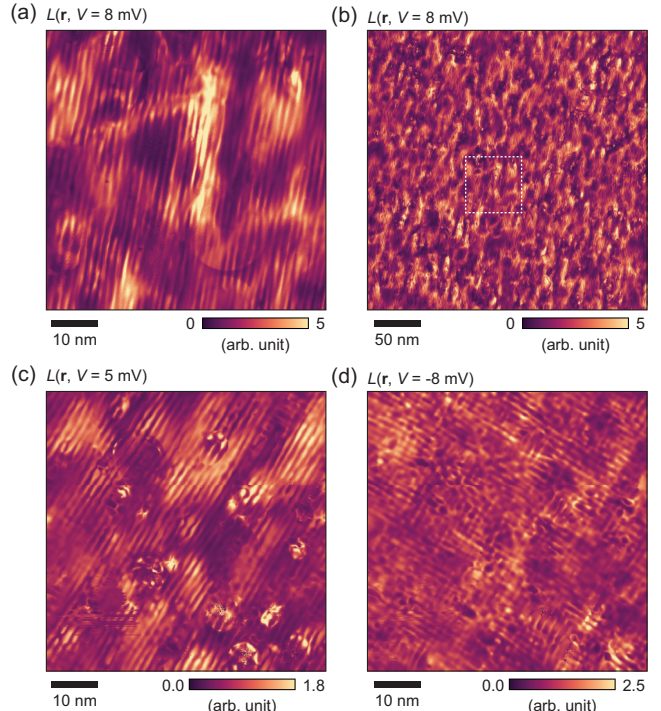


FIG. 7. Source $L(\mathbf{r})$ images used to obtain the Fourier transform results displayed in Figs. 2 and 3. (a) and (b) Images used to obtain $\mathcal{F}[L(\mathbf{r})]$ in Figs. 2(a) and 2(b), respectively. The smaller field-of-view is marked in the larger one with a white dashed line. (c) and (d) Images used to obtain those in Figs. 3(a) and 3(b), respectively.

distribution that is more consistent with C_{4v} symmetry as a negative energy.

Appendix C: Lorentzian fitting for charge stripe order parameter

Fitting to the Fourier magnitude sampled along linecut L0 and shown in Fig. 2(c) was performed using a skewed Lorentzian lineshape [34] atop an exponentially decaying background:

$$I(q) = \frac{A}{\pi} \left[\frac{1}{\gamma \left[1 + \frac{|q - q_{\text{str}}|^2}{\gamma^2 (1 + \text{sgn}(q - q_{\text{str}}))} \right]} \right] + e^{-\lambda q} + c. \quad (\text{C1})$$

Fitting to the data sampled along a linecut passing through $\mathbf{q}_{\text{str},a}$, but perpendicular to it, was performed using a simple Lorentzian lineshape:

$$I(q) = \frac{A}{\pi} \left[\frac{\gamma}{(q - q_{\text{str}})^2 + \gamma^2} \right] + c. \quad (\text{C2})$$

The constant c accounts for the uniform noise floor in q space. In each case γ describes the fluctuations of the order and a coherence length can be obtained as $\xi = 1/\gamma$. Because the charge stripe order breaks rotational symmetry, two coherence lengths, perpendicular and parallel to the stripe orientation, are needed for a full description. These are extracted from the linecut L0 and the perpendicular cut through $\mathbf{q}_{\text{str},a}$ respectively. The fitted functions give the values $\xi_{\perp} \approx 9.07 \text{ nm}$ and $\xi_{\parallel} \approx 20.33 \text{ nm}$.

Appendix D: Microscopic registry of atomic and charge stripe modulations

In Fig. 2 above we observe from the FFTs of L images that the periodicity of the stripe order is incommensurate with the atomic lattice. Here we show the microscopic correspondence in r -space between the stripe modulations and the lattice. Because the atomic lattice modulations are not readily observable in topography images, we enhanced them using an inverse Fourier transform technique. Figure 7(a) shows a topography image and Fig. 7(b) shows its FFT with the signals around each of the Bragg vectors enhanced 50-fold for clarity. We filter for these signals, and multiple them by a factor of 500 before inverse transforming them and adding them back to the original topography. We then inspect two small fields-of-view, in boxes labeled B1 and B2 in Fig. 7(a). We compare the manipulated topography maps $T^*(\mathbf{r})$ shown in Fig. 7(c) and 7(d), with the simultaneously acquired conductance maps $L(\mathbf{r}, V = 8 \text{ mV})$ shown in Fig. 7(e) and 7(f). Figures 7(g) and 7(h) show linecuts through both $T^*(\mathbf{r})$ and $L(\mathbf{r})$ images, with the local maxima of L marked by dashed lines. These comparisons show that

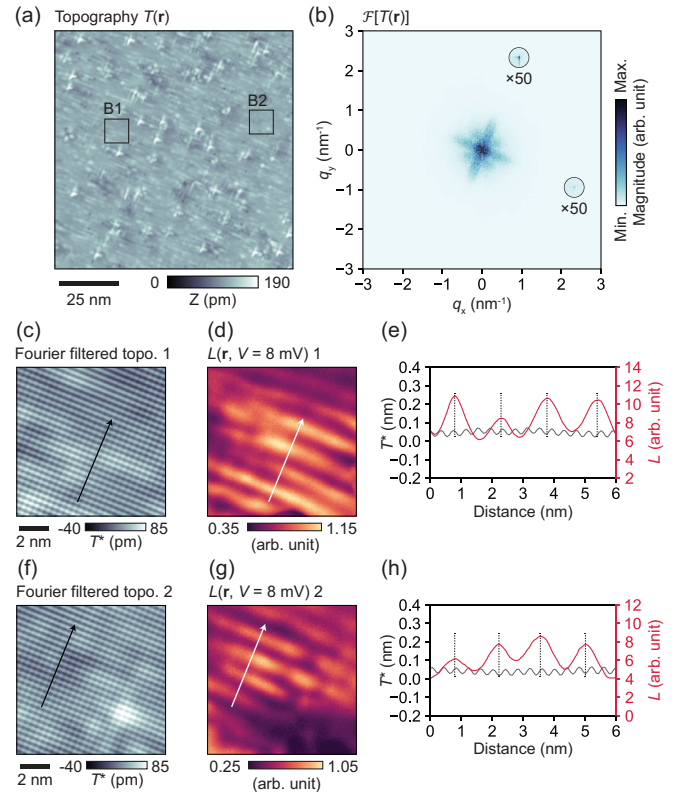


FIG. 8. Microscopic registry of atomic and charge stripe modulations. (a) Topography ($V = 30 \text{ mV}$, $I_{\text{set}} = 100 \text{ pA}$) and (b) its FFT, with the signals around the locations of the Bragg vectors enhanced for clarity. (c) and (d) Zoom-in views of topography in boxes B1 and B2 marked in (a), and with the atomic corrugations enhanced 500-fold using inverse Fourier filtering, the result of which we call $T^*(\mathbf{r})$. (e) and (f) Simultaneously measured conductance L (using $V_{\text{mod}} = 0.5 \text{ mV}$) in the same fields-of-view. (g) and (h) Linecuts through $T^*(\mathbf{r})$ and $L(\mathbf{r})$ along the paths marked in (c) and (d), respectively.

there is no strict registry between the charge stripe and atomic corrugations, and that they are microscopically incommensurate.

Appendix E: SC coherence peak fitting

In Fig. 5(f) we show results of fitting to the upper and lower coherence peaks seen in $\frac{dI}{dV}(V)$ curves. The coherence peaks appear to be qualitatively unlike those of the Dynes curve expected in the BCS paradigm. (The tail of each coherence peak falls off too quickly.) Because of this we resort to using a phenomenologically motivated fitting function. We use separate functions for the upper and lower coherence peaks (UCP and LCP), each a Lorentzian lineshape atop a hypertangent background, written as

$$\rho(V) = \frac{A_{\text{UCP}}}{\pi} \left[\frac{\gamma_{\text{UCP}}}{(eV - \Delta_{\text{UCP}})^2 + \gamma_{\text{UCP}}^2} \right] + B_{\text{UCP}} \tanh(w_{\text{UCP}} (eV - E_{\text{UCP,tanh}})) \quad (\text{E1})$$

for the UCP, and similarly but with a reversed energy scale for the LCP. The assessed value of the gap parameter is then $\Delta(r) = [| \Delta_{\text{UCP}}(r) | + | \Delta_{\text{LCP}}(r) |] / 2$.

Appendix F: DFT calculations

The calculation of the electronic structure of NaAlSi was performed using DFT as implemented in the Vienna *ab initio* simulation package (VASP) [35, 36]. All the calculations were performed with the projector-augmented wave (PAW) [37] pseudopotential and the generalized

gradient approximation (GGA) in the form of Perdew-Burke-Ernzerhof (PBE) [38, 39]. The plane-wave cut-off energy was 450 eV and a Γ -centered $12 \times 12 \times 12$ k -mesh was used to describe the electronic structure. The experimental lattice parameters and atomic positions for NaAlSi are used, with values of $a_0 = 4.125 \text{ \AA}$ and $c_0 = 7.374 \text{ \AA}$ [23]. Based on the DFT electronic band structure, we construct the atomic Wannier functions using 16 orbitals including Al s , p and Si s , p [40]. For the surface spectral function, we utilize the iterative Green's function [41] to compute the (001) surface bands of NaAlSi by constructing a semi-infinite slab using the Wannier tight-binding Hamiltonian as implemented in the WannierTools package [42]. We also perform a DFT calculation of an 11-layer NaAlSi slab with Na terminations to find good agreement in the surface band results between the two methods.